Unveiling spin-flip processes in a neutral quantum dot using an anisotropic photonic structure

Romain Fons, Saptarshi Kotal, Alberto Artioli, Joël Bleuse, Jean-Michel Gérard, and Julien Claudon*
"Nanophysique et semiconducteurs" Group, Université Grenoble Alpes, CEA, IRIG, PHELIQS, F-38000 Grenoble, France

(Received 25 December 2020; revised 21 January 2022; accepted 9 March 2022; published 30 March 2022)

We introduce a method to investigate excitonic spin flips in a neutral quantum dot (QD) that is driven nonresonantly. By inserting the QD in an anisotropic photonic structure, one creates an imbalance between the radiative decay rates of the two bright excitons. Direct spin flips between the bright excitons as well as indirect ones (*via* a dark exciton) mix the level populations and profoundly affect the degree of linear polarization of the excitonic emission. Measuring this quantity under continuous wave optical excitation yields the spin-flip rate over a broad range of excitation powers. Additional time-resolved experiments allow disentangling the contributions of bright-bright and dark-bright spin flips in the low-excitation regime. After providing theoretical background, we demonstrate the method on a self-assembled InAs QD embedded in a GaAs photonic wire featuring an elliptical cross section. For low-excitation power and at $T = 5$ K, bright-bright spin flips are much slower than dark-bright spin flips, which, in turn, remain much slower than the radiative decays. Upon increasing the temperature, we observe a superlinear increase in the bright-bright spin-flip rate which completely reverses the rate hierarchy above $T = 50$ K. Moreover, polarization measurements reveal a dramatic increase in the spin-flip rate with the pumping power. Our findings are relevant to spontaneous emission control by anisotropic photonic structures and to the spectral coherence of QD-based quantum light sources.

DOI: 10.1103/PhysRevB.105.115308

Semiconductor quantum dots (QDs) are solid-state artificial atoms with appealing assets for quantum photonics [1]. Many efforts are, thus, devoted to investigate in detail their optical properties. In a neutral QD, the spin degree of freedom of electrons and holes gives birth to the fine structure of excitonic levels, which comprise two bright (i.e., optically active) and two dark states [2]. The lifetime and coherence of these levels are of primary importance for the emission of nonclassical states of light, including the emission of single photons [3], entangled photon pairs [4], and photonic cluster states [5]. In this context, spin-flip processes are generally detrimental. Indeed, they cause an incoherent interconversion between the excitonic states, thereby directly limiting their lifetime. Previous works have revealed a strong dependence of the spin-flip rate over the QD excitation strategy: Resonant optical driving is generally more favorable [6,7] than nonresonant excitation [8]. Moreover, spin-flip processes are sample dependent: Identical material systems probed under similar experimental conditions can show very different behaviors (see, for example, Refs. [9,10]). Finally, several mechanisms can generate spin flips for the localized charge carriers trapped in a QD. These include the coupling to crystal vibrations—phonons [11,12], to charge carriers located in the QD environment [13] or to nuclear spins through the hyperfine interaction [14].

Nonresonant optical excitation of the QD can be used to emulate the electrical driving which is employed in practical sources of quantum light [15–17]. After a nonresonant optical excitation pulse, dark-bright spin flips are directly apparent in the time-resolved decay of photoluminescence [18]. The investigation of bright-bright spin flips is more challenging. Indeed, it generally relies on the selective excitation of one of the bright states, combined with state-selective detection. For neutral QDs, nonresonant excitation unfortunately offers a much poorer spin selectivity [8] than resonant driving [6,7,19].

In this paper, we introduce a method to probe excitonic spin flips in a neutral QD that is driven nonresonantly. A photonic structure provides an optical anisotropy which generates a large imbalance between the radiative decay rates of the two bright excitons. Bright-bright and dark-bright spin flips mix the excitonic level populations and strongly impact the degree of linear polarization of the excitonic emission. Measuring this quantity gives access to the spin-flip rates over a broad range of excitation power. In the low-power excitation regime, additional time-resolved measurements allow disentangling the contributions of bright-bright and dark-bright spin flips. We demonstrate this method on a self-assembled InAs QD inserted in a GaAs photonic wire featuring an elliptical cross section. Experiments reveal, in particular, a superlinear increase in the bright-bright spin-flip rate with the temperature. Moreover, polarization measurements show that spin-flip processes strongly depend on the nonresonant excitation power.

The article is organized as follows. Section I presents the theoretical background behind polarization measurements and discusses the experimental dependence of spin flips on the temperature and on the excitation power. Section II is dedicated to time-resolved measurements, performed in the low-power regime and for various temperatures. We finally conclude and examine the implications of this paper for spontaneous emission control in anisotropic photonic structures

*julien.claudon@cea.fr

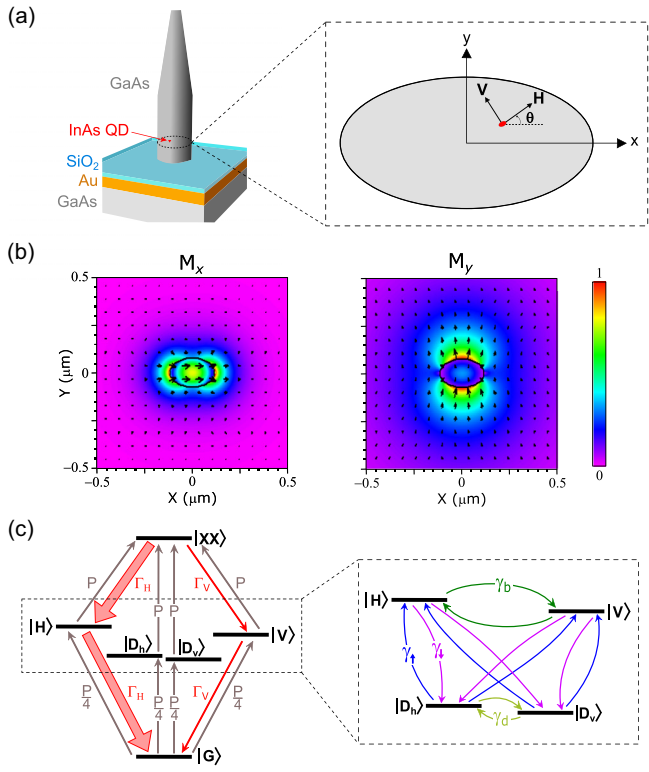

FIG. 1. (a) A neutral self-assembled QD is inserted in an anisotropic photonic structure, here a photonic wire antenna having an elliptical cross section. The sketch on the right shows the relative orientation of the QD dipoles H and V with respect to the photonic axes x and y. (b) Calculated map of the transverse electrical field (i.e., on the xy plane) associated with the guided modes M_x and M_y. The simulation is performed for an infinitely long wire with major and minor diameters of $d_x = 230$ and $d_y = 160$ nm, respectively (operation wavelength 920 nm). The black arrows indicate the orientation of the local polarization. (c) Left: QD level scheme showing the pumping model that describes nonresonant cw excitation and radiative decays. Photonic anisotropy creates a pronounced imbalance between the spontaneous emission rates Γ_H and Γ_V. Right: spin-flip transitions between excitonic levels.

and for the spectral coherence of QD-based quantum light sources.

I. PROBING SPIN FLIPS WITH POLARIZATION MEASUREMENTS

A. Theoretical background

1. A neutral QD in an anisotropic photonic structure

Figure 1(c) shows the level scheme associated with the s-shell excitonic complexes hosted by a neutral self-assembled QD. We consider here QDs which display a sufficient in-plane symmetry (in terms of morphology and strain field) so that the valence-band mixing between the heavy-hole (hh) and light-hole (lh) states is negligible (more details on the QDs investigated in this paper in Sec. I B). Starting from the QD ground state $|G\rangle$, excitonic states are then constructed with a hh state ($|\Downarrow\rangle$ or $|\Uparrow\rangle$ corresponding to a total hole angular momentum projection $-3/2$ and $+3/2$, respectively) and a conduction-band electron state ($|\downarrow\rangle$ or $|\uparrow\rangle$ corresponding to a spin projection $-1/2$ and $+1/2$, respectively). The resulting four exciton states can be classified depending on the projection J_z of the total angular momentum along the growth direction. Bright excitons, featuring $J_z = \pm 1$, can recombine radiatively and decay to $|G\rangle$, whereas dark excitons, characterized by $J_z = \pm 2$, are not optically active. Dark excitons are at lower energy than the bright ones, typically by a few hundreds of μeV. In general, structural or strain anisotropies lift the degeneracy of the two bright excitonic levels. The corresponding states $|H\rangle = \frac{1}{\sqrt{2}}(|\downarrow\Uparrow\rangle - |\uparrow\Downarrow\rangle)$ and $|V\rangle = \frac{1}{\sqrt{2}}(|\downarrow\Uparrow\rangle + |\uparrow\Downarrow\rangle)$ are separated by a fine-structure splitting s_b, typically in the few μeV–100-μeV range. The two dark excitonic states $|D_h\rangle = \frac{1}{\sqrt{2}}(|\uparrow\Uparrow\rangle - |\downarrow\Downarrow\rangle)$ and $|D_v\rangle = \frac{1}{\sqrt{2}}(|\uparrow\Uparrow\rangle + |\downarrow\Downarrow\rangle)$ are also splitted; the corresponding energy difference s_d is on the order of a few μeV. Finally, the biexciton state $|XX\rangle$ corresponds to the pseudospin configuration $|\downarrow\uparrow\Downarrow\Uparrow\rangle$.

The four states $|XX\rangle$, $|H\rangle$, $|V\rangle$, and $|G\rangle$ form a diamondlike level structure connected by radiative transitions. The optical transitions $|XX\rangle \leftrightarrow |H\rangle$ and $|H\rangle \leftrightarrow |G\rangle$ feature a linear optical dipole oriented along the H direction, whereas the dipole associated with $|XX\rangle \leftrightarrow |V\rangle$ and $|V\rangle \leftrightarrow |G\rangle$ is oriented along the V direction. H and V are mutually orthogonal, and we suppose that all transitions feature identical oscillator strengths. However, the rates Γ_H and Γ_V associated with the spontaneous emission (SE) decays $|H\rangle \rightarrow |G\rangle$ and $|V\rangle \rightarrow |G\rangle$ might differ due to a photonic anisotropy. The biexciton level decays with the SE rate $\Gamma_{XX} = \Gamma_H + \Gamma_V$.

As illustrated in Fig. 1(c), the four excitonic states can be connected by nonradiative spin-flip processes. To simplify the analysis, we make the following assumptions: (i) The two paths associated with a direct spin flip between the bright states $|H\rangle \rightarrow |V\rangle$ and $|V\rangle \rightarrow |H\rangle$ feature the same rate γ_b. (ii) Similarly, the direct spin flip between the two dark states $|D_h\rangle$ and $|D_v\rangle$ is characterized by a single rate γ_d. (iii) The four dark-bright spin-flip channels are characterized by a single rate $\gamma_\uparrow$. (iv) Similarly, the reverse processes are also characterized by a unique rate $\gamma_\downarrow$. This model holds as long the energy splittings s_b and s_d are much smaller than the thermal energy $k_B T$ (k_B is the Boltzmann constant and T is the temperature).

In this paper, we integrate the QD in an anisotropic photonic environment to reveal spin-flip processes. As schematized in Fig. 1(a), we consider a photonic wire antenna [20] featuring an elliptical cross section, whose major and minor axes are aligned along the x and y directions, respectively. The wire features a needlelike top taper [21] and stands on a SiO_2-Au bottom mirror [22]. This structure supports two guided modes M_x and M_y with orthogonal linear polarizations oriented along x and y, respectively. A linear optical dipole aligned along the x (y) direction feeds M_x (M_y) with a SE rate Γ_x (Γ_y). These rates can be determined thanks to a Fabry-Pérot model [23], which first considers the emission in an infinitely long wire and next includes the reflections on the wire extremities. Such an analysis shows that the imbalance between Γ_x and Γ_y ($\Gamma_x > \Gamma_y$) arises from two contributions. First, in an infinitely long wire, M_x is more confined in the waveguide than M_y due to the elliptical cross section [9] [see Fig. 1(b)]. Second, the bottom mirror leads to a two-wave interference

that depends on the mode. Indeed, M_x and M_y feature different effective indices, leading to distinct enhancement factors for the SE rates. In practice, the imbalance between Γ_x and Γ_y can be controlled by adjusting the ellipticity of the section and by controlling the height of the QD with respect to the bottom mirror.

To account for a possible misalignment between the QD dipoles and the photonic axes, we introduce θ, the angle between H and x. The SE rates Γ_H and Γ_V reads

$$\Gamma_H = \cos^2(\theta)\Gamma_x + \sin^2(\theta)\Gamma_y \tag{1}$$

$$\Gamma_V = \sin^2(\theta)\Gamma_x + \cos^2(\theta)\Gamma_y. \tag{2}$$

In these expressions, the first term is associated with the emission into M_x, whereas the second one is associated with the emission into M_y. The imbalance in SE rates is maximal for $\theta = 0$ and completely vanishes for $\theta = \frac{\pi}{4}$. We next discuss the connection between the polarization of excitonic emission and spin-flip processes for a continuous wave excitation.

2. Polarization of the exciton emission

The excitonic (X) emission is the sum of the radiative decays $|H\rangle \rightarrow |G\rangle$ and $|V\rangle \rightarrow |G\rangle$. We consider an incoherent excitation of levels $|H\rangle$ and $|V\rangle$ and suppose that s_b largely exceeds the homogeneous linewidth of both levels. One can then neglect interference between the two emission channels. We collect the two contributions (without spectral resolution) and introduce a linear polarizer in the free-space collection path. The transmitted intensity reads

$$I_X(\alpha) = \cos^2(\alpha)I_x + \sin^2(\alpha)I_y + \sin(2\alpha)I_{xy}, \tag{3}$$

where α is the angle between the polarizer axis and the x axis; I_x (I_y) is the intensity funneled in mode M_x (M_y); I_{xy} accounts for the mixing of the electric fields of M_x and M_y on the polarizer axis. Thanks to the antenna top taper [21], the output beams associated with M_x and M_y are directive enough to be fully intercepted by free-space optics featuring a large numerical aperture. The far-field collection efficiencies of M_x and M_y are then identical. Within a common multiplying constant, I_x, I_y, and I_{xy} then read

$$I_x = \Gamma_x[\cos^2(\theta)\bar{n}_H + \sin^2(\theta)\bar{n}_V] \tag{4}$$

$$I_y = \Gamma_y[\sin^2(\theta)\bar{n}_H + \cos^2(\theta)\bar{n}_V] \tag{5}$$

$$I_{xy} = \sqrt{\Gamma_x\Gamma_y}\cos(\varphi)\sin(\theta)\cos(\theta)[\bar{n}_H - \bar{n}_V]. \tag{6}$$

Here, $\bar{n}_H$ and $\bar{n}_V$ are the steady-state populations of levels $|H\rangle$ and $|V\rangle$, respectively. φ is the phase shift between M_x and M_y acquired during propagation from the QD section to the upper end of the wire. It arises because these two guided modes feature different effective indices. To obtain the expressions given above, one neglects interference terms between the emission of H and V dipoles, which is valid when s_b exceeds the homogeneous linewidth of levels $|H\rangle$ and $|V\rangle$. The degree of linear polarization of the X emission is defined as

$$L_X = \frac{I_{\max} - I_{\min}}{I_{\max} + I_{\min}}, \tag{7}$$

where the maximum (minimum) intensity $I_{\max}$ ($I_{\min}$) is obtained for the angle $\alpha_{\max}$ ($\alpha_{\min}$). We use here the convention $\alpha_{\min}, \alpha_{\max} \in [-\frac{\pi}{2}, \frac{\pi}{2}]$. As expected, the direction of maximum transmitted intensity is found in the vicinity of the strong photonic axis x: $\alpha_{\max}$ is the angle in $]-\frac{\pi}{4}, \frac{\pi}{4}[$ given by

$$\alpha_{\max} = \frac{1}{2}\arctan\frac{2I_{xy}}{I_x - I_y}. \tag{8}$$

To proceed, we determine steady-state excitonic populations under cw nonresonant excitation. We suppose that during their relaxation and capture by the QD, excited carriers lose any spin polarization, similar to Ref. [8]. We additionally consider an ambipolar excitation of the QD [24,25] and note P the capture rate of an electron-hole pair by the QD. The four ground-state-to-exciton transitions are pumped with the same rate $P/4$, whereas exciton-to-biexciton transitions are pumped with the rate P [Fig. 1(c)]. The equation system governing steady-state populations is discussed in Appendix A. One finds that the steady-state populations of dark excitonic states are equal and that dark-dark spin flips do not impact steady-state populations. An analytical expression for $(\bar{n}_H/\bar{n}_V)$ is given in Appendix A. Combined with Eqs. (3)–(7), it yields a general expression of L_X.

To showcase the sensitivity of L_X to spin-flip processes, we first consider the case $\theta = 0$, which leads to simple analytical expressions. The radiative decay $|H\rangle \rightarrow |G\rangle$ then only feeds the photonic mode M_x with a rate Γ_x, whereas the decay $|V\rangle \rightarrow |G\rangle$ only feeds M_y with a rate Γ_y. For $\theta = 0$, Eq. (6) leads to $I_{xy} = 0$: the polarization eigenaxes correspond to the photonic axes x and y. We consider two limit cases: low-power and high-power cw excitation. The corresponding asymptotic values of $(\bar{n}_H/\bar{n}_V)$ are given in Appendix A.

In the low-power limit, the excitation rate is much smaller than all other rates ($P \ll \gamma_b,\ \gamma_{\downarrow,\uparrow},\ \Gamma_{H,V}$). The QD is, thus, predominantly in the ground state; $|H\rangle$ and $|V\rangle$ are excited from this state with the same rate but decay with distinct radiative rates, leading to

$$L_X = \frac{\gamma_{b\downarrow}(\Gamma_x - \Gamma_y)}{\Gamma_x\Gamma_y + \gamma_{b\downarrow}(\Gamma_x + \Gamma_y)}. \tag{9}$$

This expression explicitly depends on the aggregate spin-flip rate $\gamma_{b\downarrow} = \gamma_b + \gamma_\downarrow$. In the absence of spin-flip ($\gamma_{b\downarrow} = 0$), $L_X = 0$. This surprising result is explained by the independence of the dynamics of $|H\rangle$ and $|V\rangle$ levels. These levels are indeed excited with the same rate and have the time to emit a photon before a new excitation event ($P \ll \Gamma_{H,V}$). This ensures a perfect balance between the intensities in the x and y channels. A finite spin-flip rate $\gamma_{b\downarrow}$ mixes the populations $\bar{n}_H$ and $\bar{n}_V$, which enables a competition between the fast and the slow decay channel, leading to the buildup of a linear polarization along the fast photonic axis x. The maximum degree of polarization is achieved when spin flips are much faster than radiative processes ($\gamma_{b\downarrow} \gg \Gamma_{H,V}$), leading to $L_X = L_X^\infty$ with

$$L_X^\infty = \frac{\Gamma_x - \Gamma_y}{\Gamma_x + \Gamma_y}. \tag{10}$$

The degree of linear polarization is, thus, very sensitive to the presence of spin-flip processes and *increases* from 0 to L_X^∞ as $\gamma_{b\downarrow}$ increases from 0 to $+\infty$.

In the opposite, high-power limit ($P \gg \Gamma_{H,V}$), the QD is predominantly found in the bi-exciton state. $|H\rangle$ and $|V\rangle$ are mainly excited by the radiative decay of $|XX\rangle$. The imbalance $\Gamma_H > \Gamma_V$ introduces a preferential pumping of $|H\rangle$, leading to

$$L_X = \frac{\left(\Gamma_x^2 - \Gamma_y^2\right) + f(P)\left(\Gamma_x^2 - \Gamma_y^2\right)}{(\Gamma_x + \Gamma_y)^2 + f(P)(\Gamma_x - \Gamma_y)^2}, \tag{11}$$

where $f(P)$ accounts for the competition between the optical excitation and the spin-flip processes,

$$f(P) = \left(\frac{P}{2\gamma_\uparrow + P}\right)\left(\frac{2\gamma_\uparrow + 2\gamma_\downarrow + P}{2\gamma_b + 2\gamma_\downarrow + P}\right). \tag{12}$$

For slow spin-flips ($\gamma_b, \gamma_{\uparrow,\downarrow} \ll P$), $f(P) = 1$ which leads to $L_X = (\Gamma_x^2 - \Gamma_y^2)/(\Gamma_x^2 + \Gamma_y^2)$. In the opposite limit of fast spin-flips (γ_b or $\gamma_{\uparrow,\downarrow} \gg P$), the effects of preferential pumping vanish: $f(P) = 0$ and one finds again $L_X = L_X^\infty$. In the high-power limit, L_X can, thus, also be used to reveal fast spin-flip processes. Contrary to the low-power case, spin flips lead here to a *reduction* of L_X from $(\Gamma_x^2 - \Gamma_y^2)/(\Gamma_x^2 + \Gamma_y^2)$ down to $(\Gamma_x - \Gamma_y)/(\Gamma_x + \Gamma_y)$. Since both expressions tend towards unity when $\Gamma_x \gg \Gamma_y$, a moderate photonic anisotropy (say Γ_x/Γ_y in the 2–6 range) is desirable to investigate spin-flip processes in the high-power limit.

We now come back to the general case of $\theta \neq 0$. First, the fast spin-flip limit identified in the previous paragraphs is general. Indeed, fast spin flips lead to $\bar{n}_H = \bar{n}_V$. Equation (6) yields $I_{xy} = 0$, which implies that the polarization eigenaxes match the photonic axes x and y. The equality of populations also directly implies $L_X = L_X^\infty$. A nonzero θ, however, impacts the values of L_X for finite spin-flip rates. Indeed, the contributions of QD dipoles to M_x and M_y are then mixed with an effect similar to the one of spin flips. In particular, when $\theta = \pi/4$, the sensitivity to spin-flip processes completely vanishes: whatever the spin-flip and pumping rates, $L_X = L_X^\infty$. To optimize the sensitivity of L_X to spin-flip processes, θ should be as close as possible to zero. From a practical point of view, the optical dipoles of an InAs QD are, in general, roughly aligned along the [110] and [1$\bar{1}$0] crystal directions [26], which, in turn, correspond to easy cleavage axis of GaAs. Aligning the photonic axes along these directions ensures moderate values for θ. In any case, even if θ is small, it is crucial to determine its value for a quantitative analysis. We finally comment on a possible deviation of the polarization eigenaxes from the photonic axes x and y. Inspection of Eq. (8) reveals that such a deviation necessitates a population imbalance ($\bar{n}_H \neq \bar{n}_V$) combined with $I_x \sim I_y$. These conditions can be achieved in the low-power limit in the presence of slow spin flips. In all other cases, deviations are generally negligible.

3. The biexciton emission as an in situ reference

The biexciton (XX) emission is the sum of the radiative decays $|XX\rangle \rightarrow |H\rangle$ and $|XX\rangle \rightarrow |V\rangle$. When the fine-structure splitting s_b largely exceeds the homogeneous linewidth of these radiative transitions, one can replace $\bar{n}_H$ and $\bar{n}_V$ by $\bar{n}_{XX}$ in Eqs. (4)–(6) to obtain

$$L_{XX} = \frac{\Gamma_x - \Gamma_y}{\Gamma_x + \Gamma_y} = L_X^\infty. \tag{13}$$

Because the XX emission originates from a single state, this value does not depend on the pumping conditions nor on the presence of excitonic spin flips. Therefore, the XX emission can be used as an *in situ* reference to assess the presence of excitonic spin flips (simply by comparing L_X to L_{XX}). Furthermore, the directions of maximum and minimum transmitted intensities correspond to the x and y axis, respectively. The polarization directions of the XX emission thus reveal the axes of the photonic structure. Finally, combined measurements of L_{XX} and $\Gamma_{XX} = \Gamma_x + \Gamma_y$ yields the photonic parameters Γ_x and Γ_y.

We finally note that the power dependence of the XX intensity I_{XX} is very sensitive to dark-bright spin flips. We focus here on the low-power part ($P \ll \Gamma_H, \Gamma_V$) and recall that $I_{XX} \propto \bar{n}_{XX}$. For slow dark-bright spin-flips ($\gamma_{\downarrow,\uparrow} \ll P$), an optical pumping effect leads to the buildup of a large dark exciton population ($\bar{n}_{D_h} + \bar{n}_{D_v} = 1/3$), which vastly exceeds the bright exciton populations. Both $\bar{n}_{XX}$ and I_{XX} are then proportional to P, a result that is not affected by the presence of bright-bright spin flips. In the opposite regime of fast dark-bright spin-flips ($\gamma_{\downarrow,\uparrow} \gg P$), the optical pumping is suppressed. All excitonic levels feature a population proportional to P, which leads to a quadratic power dependence for $\bar{n}_{XX}$ and I_{XX}.

B. Experimental results

We now turn to the experimental demonstration of the proposed method. We consider self-assembled InAs QDs that are grown on [001] GaAs. The QDs are formed during the fast (1s) deposition of 2.0 monolayers of InAs, immediately followed by GaAs capping. These growth conditions lead to a QD areal density of a few 100 μm^{-2} and an ensemble luminescence that peaks around 920 nm. Such QDs exhibit weak polarization, pointing towards balanced oscillator strengths for the H and V dipoles [26]. In addition, the observation of a pronounced inhibition of SE in tiny photonic nanowires [27] and absorption measurements in waveguides [28] both indicate a negligible *hh-lh* valence-band mixing. We note that other growth conditions can lead to significantly different properties, especially for low-density samples [26,29].

These QDs are embedded in a GaAs photonic wire antenna that was fabricated in the same batch as the one investigated in Refs. [27,30,31]. The photonic wire is approximately 3-μm high, features a needlelike taper and stands on a planar mirror. The QDs are located 80 nm above the bottom mirror, and their lateral position in the wire section is random. Due to a slight anisotropy in the etching process, the cylindrical base exhibits for some structures an elliptical cross section. We focus here on a structure with a major diameter of 230 nm and a minor diameter of 160 nm. For an on-axis emitter, FDTD simulations that take into account the reflection on the bottom mirror predict an optical anisotropy $\Gamma_x/\Gamma_y = 3.8$, suitable for probing spin-flip processes both in the low-power and in the high-power limits. In addition, numerical simulations show that other modes than M_x and M_y can be safely neglected.

The antenna chip is mounted on the cold finger of a helium flow cryostat with optical access. Nonresonant excitation is provided by a continuous-wave Ti:sapphire laser, which is focused on a single nanowire with a microscope objective

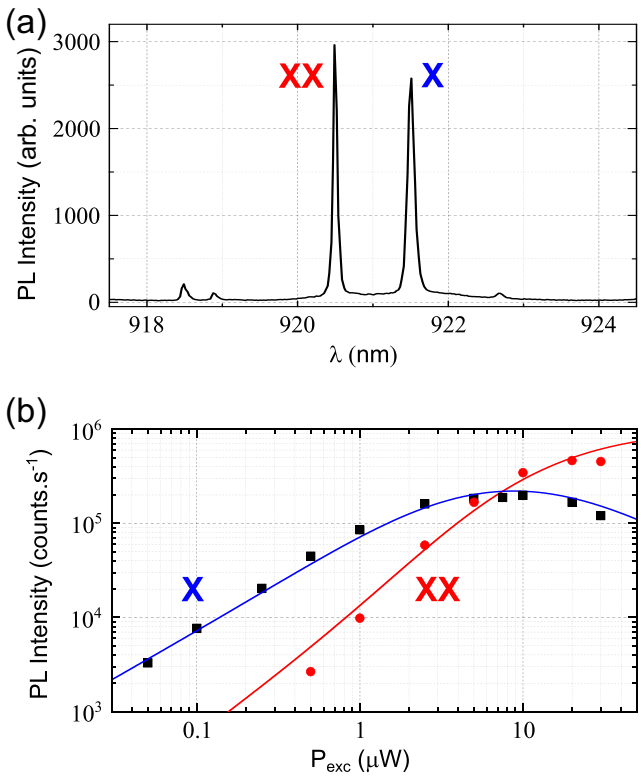

FIG. 2. (a) Microphotoluminescence spectrum recorded on the CCD ($T = 5$ K, cw excitation, $P_{\rm exc} = 2.5$ μW). The fine structure of the exciton (X) and biexciton (XX) emission lines is not resolved here. (b) Spectrally integrated intensities of the X (squares) and XX (disks) emission lines as a function of the pumping power $P_{\rm exc}$ (log-log plot). The polarizer is oriented along the x direction and spectral integration is performed with an APD. The solid lines are theoretical predictions using the same parameters than for the analysis of polarization data shown in Figs. 3(c) and 3(d).

(numerical aperture 0.75). The laser is linearly polarized; it is tuned to 835 nm to generate electrons and holes in the two-dimensional continuum of the QD wetting layer. The QD luminescence signal is collected by the same objective. Spectral resolution is provided by a grating spectrometer (1200 grooves/mm; focal length 64 cm) equipped with a silicon CCD camera and a silicon avalanche photodiode (APD). Polarization analysis is performed with a rotating $\lambda/2$ wave plate and a fixed linear polarizer located before the spectrometer. We have checked that rotating the polarization of the excitation laser with respect to the sample does not affect the polarization of the QD emission.

We illustrate the method on a particular QD, whose microphotoluminescence spectrum is shown in Fig. 2(a) (cw excitation power $P_{\rm exc} = 2.5$ μW, $T = 5$ K). The exciton line (X) line is centered at 921.44 nm and the biexciton (XX) emission is centered at 920.46 nm. The two lines are well separated and stand on a clean background. In the low-power regime, the spectrally integrated intensities of the X and XX lines scale as $P_{\rm exc}^{1.0}$ and $P_{\rm exc}^{1.9}$, respectively [Fig. 2(b)]. Spectral resolution is not sufficient to directly reveal the fine structure of the two lines. However, X and XX display opposite spectral shifts when rotating the $\lambda/2$ wave plate (not shown). This establishes X and XX belong to the same neutral QD and yields the fine-structure splitting $s_b = 34 \pm 2$ μeV.

We first focus on the polarization analysis of the XX emission line. Raw polarization data are shown in Fig. 3(a) for $P_{\rm exc} = 5$ μW and $T = 5$ K. In this polar plot, the analysis angle is $\alpha = 2\alpha_{\lambda/2}$, where $\alpha_{\lambda/2}$ is the angle of the $\lambda/2$ wave plate. The transmitted intensity is fit to $I_0 C(\alpha)\{L_{XX}\cos[2(\alpha - \alpha_{XX}^{\rm max})] + 1\}$. Here, I_0 is a global intensity scaling factor; L_{XX} is the degree of polarization of the XX emission and $\alpha_{XX}^{\rm max}$ is the direction of maximum transmitted intensity; $C(\alpha) = 1 + c_0\{\cos[(\alpha - \alpha_c)/2] - 1\}$ accounts for a residual experimental imperfection. A slight defect in the parallelism of the wave plate induces a displacement of the optical spot on the APD pixel when the wave plate is rotated. As apparent in Fig. 3(a), the correction is small: c_0 typically amounts to a few percent. Figure 3(c) shows that L_{XX} does not depend on $P_{\rm exc}$. This is also the case for $\alpha_{XX}^{\rm max}$ as evidenced in Fig. 3(d). We repeated experiments for various temperatures (up to 50 K). Again, L_{XX} and $\alpha_{XX}^{\rm max}$ are constant within experimental uncertainties. We use in the following the average value $L_{XX} = 0.57 \pm 0.02$ as a reference; $\alpha_{XX}^{\rm max} = 120 \pm 2^\circ$ indicates the direction of x, the strong photonic axis.

Figure 3(b) shows raw polarization data for the X line in the low-power regime ($P_{\rm exc} = 50$ nW) and in the saturation regime ($P_{\rm exc} = 20$ μW) for $T = 5$ K. In contrast to the biexciton case, the polarization of the exciton emission strongly depends on the pumping power. Quantitative analysis is performed similarly as in the biexciton case (one replaces L_{XX} and $\alpha_{XX}^{\rm max}$ by L_X and $\alpha_X^{\rm max}$ in the fit function). L_X is plotted against $P_{\rm exc}$ in Fig. 3(c). For the measurement with the lowest excitation power, $L_X = 0.23$. This value, well below $L_{XX} = L_X^\infty$, is indicative of slow spin-flips ($\gamma_b + \gamma_\downarrow \ll \Gamma_{H,V}$) and small θ. Upon increasing $P_{\rm exc}$, L_X increases to approach asymptotically L_X^∞ for large powers. In the high-power limit, this is the signature of fast spin-flips (γ_b or $\gamma_{\downarrow,\uparrow} \gg \Gamma_{H,V}$). At this stage, we can already conclude that, at least, one of the spin-flip rates strongly increases with the pumping power. As discussed in Sec. IA3, further insight on spin-flip processes is provided by the power dependence the XX intensity. Experimentally, we obtain a low-power dependence that is nearly quadratic [$\propto P_{\rm exc}^{1.93}$ for $P_{\rm exc}$ in the 0.5–5 μW range, see Fig. 2(b)]. This is the signature that the dark-bright spin-flip rates exceed the pumping rate P in this power range.

The power dependence of the polarization angle $\alpha_X^{\rm max}$ is shown in Fig. 3(d). For the measurement with the lowest power ($P_{\rm exc} = 50$ nW), $\alpha_X^{\rm max} - \alpha_{XX}^{\rm max} = 12^\circ$, confirming that spin-flip processes are slow in the low-power regime. Additionally, this reveals a misalignment between the QD and the photonic eigenaxes ($\theta \neq 0$). For the largest excitation power ($P_{\rm exc} = 30$ μW), $\alpha_X^{\rm max}$ is equal to $\alpha_{XX}^{\rm max}$ within experimental errors. This observation is consistent with fast spin flips, which align the polarization eigenaxes of the X emission on the photonic axes x and y.

We now perform a quantitative analysis. To infer spin-flip rates from polarization data, one should determine the set of fixed parameters $\{\Gamma_x, \Gamma_y, \theta, \cos(\varphi)\}$. We achieve this by performing additional time-resolved measurements that will be discussed in the second part of the article. The whole procedure is summarized below. The time decay of the biexciton is $\Gamma_{XX} = \Gamma_H + \Gamma_V = \Gamma_x + \Gamma_y$. Combined with the

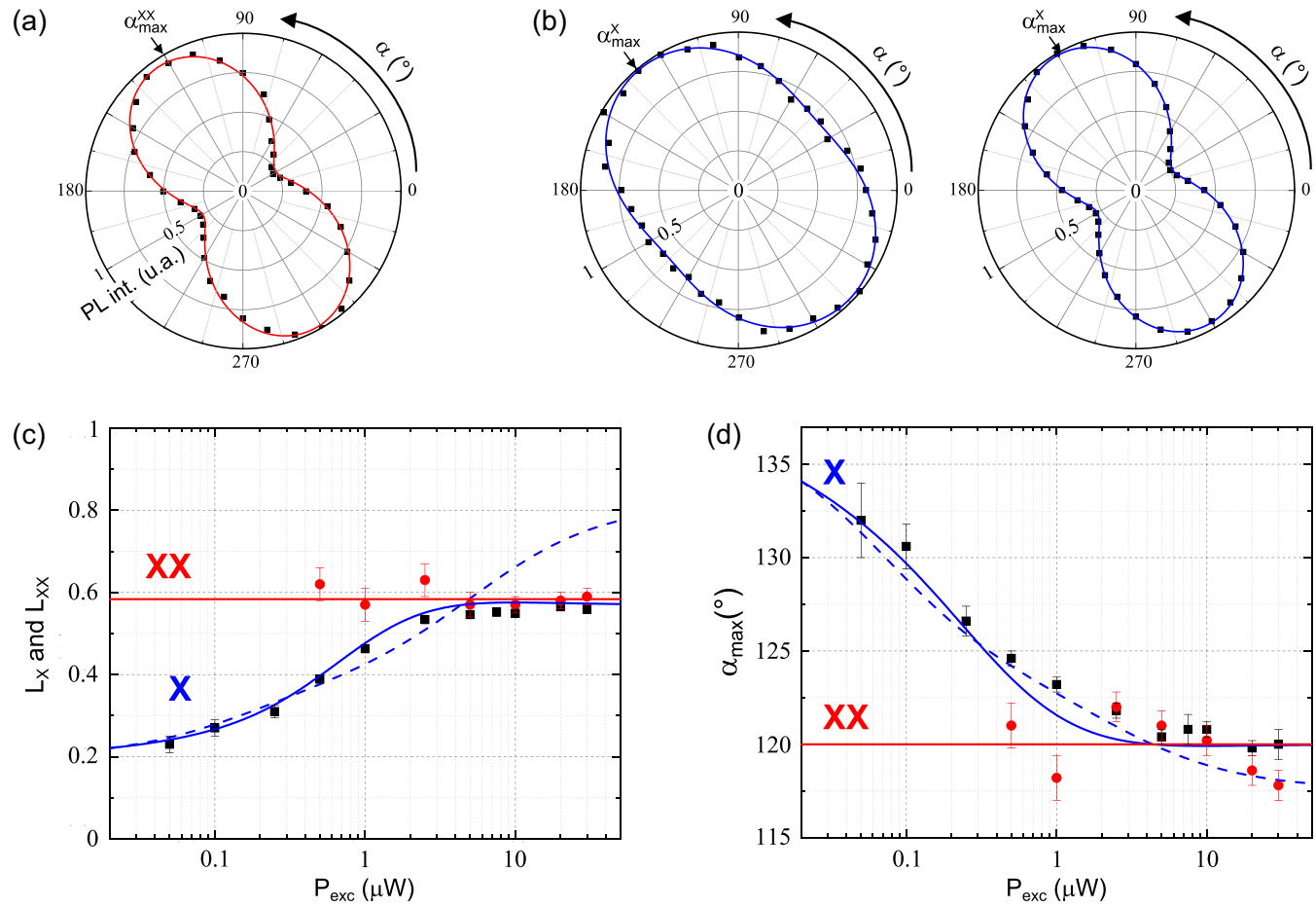

FIG. 3. (a) Raw polarization data of the XX line for an excitation power $P_{\text{exc}} = 5\ \mu$W. The solid line is a fit that yields the degree of linear polarization L_{XX} and the direction of polarization $\alpha_{XX}^{\max}$ (see the text for details). (b) Raw polarization data for the X line at small ($P_{\text{exc}} = 50$ nW, left) and large ($P_{\text{exc}} = 20\ \mu$W, right) excitation power. The solid lines are fits that yield L_X and $\alpha_X^{\max}$. All measurements are performed under cw excitation at $T = 5$ K. (c) L_{XX} (disks) and L_X (squares) versus P_{exc} (lin-log plot). (d) $\alpha_{XX}^{\max}$ (disks) and $\alpha_X^{\max}$ (squares) versus P_{exc}. Within experimental errors, L_{XX} and $\alpha_{XX}^{\max}$ are constant with a mean value that appears as a solid red line. In (c) and (d), solid blue lines are computed assuming spin-flip rates which increase with P_{exc}; blue dashed lines are computed assuming constant spin-flip rates (see the text for details).

measured L_{XX}, this yields Γ_x and Γ_y. From the experimental values $\Gamma_{XX} = 1.30 \pm 0.02$ ns^{-1} and $L_{XX} = 0.57 \pm 0.02$, we determine $\Gamma_x = 1.02 \pm 0.02$ and $\Gamma_y = 0.28 \pm 0.01$ ns^{-1}. In addition, $\Gamma_H - \Gamma_V$ can be deduced from the time-decay measurement of the excitonic line in the slow spin-flip regime [see Eqs. (B1) and (B2) in Appendix B]. We then use the relation $\cos(2\theta) = (\Gamma_H - \Gamma_V)/(\Gamma_x - \Gamma_y)$ to determine θ. The experimental value of $\Gamma_H - \Gamma_V = 0.66\ \pm 0.02$ ns^{-1} leads to $\theta = 13^{+1}_{-2}{}^{\circ}$. Finally, polarization analysis in the slow spin-flip regime yields $\cos(\varphi)$ and provides an upper limit for θ, which is taken into account in the uncertainty given above. We extrapolate low-power data to obtain the zero-power limit of the degree of linear polarization and of the polarization direction, $L_X(0)$ and $\alpha_{\max}(0)$, respectively. Measurements at 5 K yield $L_X(0) = 0.20 \pm 0.01$ and $\alpha_{\max}(0) = 17 \pm 2^{\circ}$ from which we deduce $\cos(\varphi) = 0.47 \pm 0.04$ and the zero-power spin-flip rate $\gamma_{b\downarrow}(0) = \gamma_b(0) + \gamma_{\downarrow}(0) = 0.01^{+0.02}_{-0.01}$ ns^{-1}.

We next aim at describing simultaneously the power-dependence of the polarization of X emission [Figs. 3(c) and 3(d)] and of X and XX intensities [Fig. 2(b)]. The power dependence of spin-flip rates is described with an empirical model. For simplicity, we assume that all spin-flip rates are equal: $\gamma_b = \gamma_b(0) + \delta(P)$, $\gamma_{\downarrow} = \gamma_{\downarrow}(0) + \delta(P)$, and $\gamma_{\uparrow} = \gamma_{\uparrow}(0) + \delta(P)$ with $\gamma_b(0) = \gamma_{\downarrow,\uparrow}(0) = \frac{1}{2}\gamma_{b\downarrow}(0)$ and $\delta(P) = \delta_1 P + \delta_2 P^2$. Polarization data ($L_X$ and $\alpha_X^{\max}$) are calculated using the model developed in Sec. I B. The quadratic term in $\delta(P)$ ensures the convergence $L_X \to L_{XX}$ for large P's [see Eq. (12)]. The intensities $I_{X,x}$ and $I_{XX,x}$ (measured when the polarizer is aligned along the x direction) are equal to $I_{X,x} = c_X \Gamma_x [\cos^2(\theta)\bar{n}_H + \sin^2(\theta)\bar{n}_V]$ and $I_{XX,x} = c_{XX}\Gamma_x \bar{n}_{XX}$. We obtain a good agreement with the complete set of experimental data using the following parameters: $P/P_{\text{exc}} = 0.075$ ns$^{-1}\ \mu$W^{-1}, $\delta_1 = 2$, $\delta_2 = 15$ ns, $(c_X\Gamma_x) = 1.7$ MHz, $(c_{XX}\Gamma_x) = 1.0$ MHz. We note that very similar results could be obtained by attributing the power dependence solely to $\gamma_{\downarrow,\uparrow}$. However, an increase in γ_b alone would be incompatible with the observed power dependence of $I_{XX,x}$. Our data cannot be reproduced with constant spin-flip rates. The dashed line in Fig. 3(c) is calculated for $\delta(P) = 0$: It completely fails to describe L_X for large P_{exc}'s. Overall, this analysis confirms the large sensitivity of spin-flip processes to the pumping power: When P_{exc} increases from 50 nW to 30 μW, at least, one of the spin-flip rates increases by more than two orders of magnitude. This is a general trend: polarization measurements

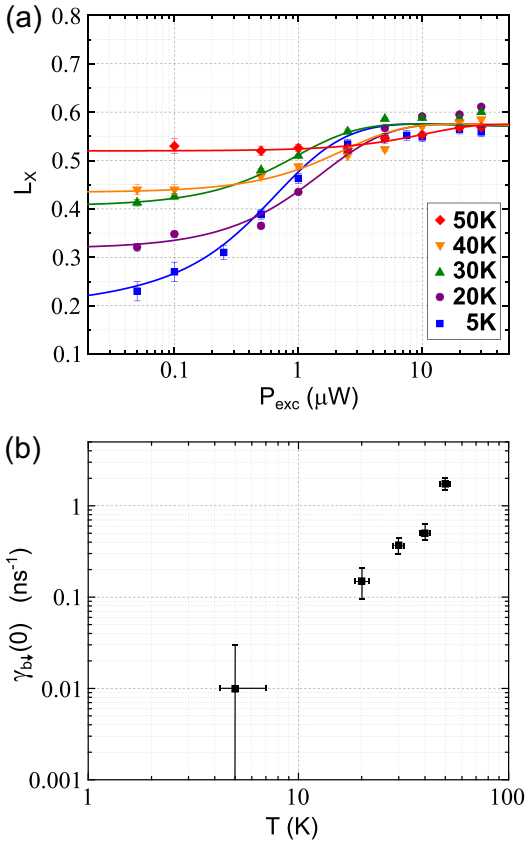

FIG. 4. (a) Degree of linear polarization of the exciton L_X as a function of the pumping power P_{exc}, measured for temperatures ranging between $T = 5$ and $T = 50$ K (lin-log plot). The solid lines are fits (see the text). (b) Zero-power value $\gamma_{b\downarrow}(0) = \gamma_b(0) + \gamma_\downarrow(0)$ extracted from the measurements shown in (a) as a function of T (log-log plot).

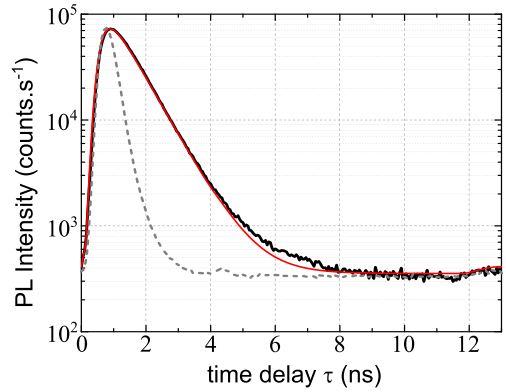

FIG. 5. Time-resolved decay of the XX emission (black line, log-lin plot) measured at 5 K. The dashed line is the measured IRF of the setup. The red line is a fit of experimental data to a single exponential decay function that is convoluted with the setup IRF.

revealed a strong increase in the spin-flip rate with P_{exc} in several other neutral QDs.

We performed similar measurements for various cryostat temperatures ranging from 5 and up to 50 K. The results are shown in Fig. 4(a). In all cases, L_X increases with P_{exc} and asymptotically approaches L_X^∞ in the high-power limit. The impact of the excitation power on the spin-flip rate remains visible, even at high temperatures. It is also clear that the low-power value of L_X tends towards L_X^∞ upon increasing T. This is a signature that the zero-power spin-flip rate $\gamma_{b\downarrow}(0) = \gamma_b(0) + \gamma_\downarrow(0)$ features a strong temperature dependence. To analyze the data, we again suppose that all spin-flip rates are equal and keep a fixed power dependence (as determined for $T = 5$ K). The two free parameters of the fit are $\gamma_{b\downarrow}(0)$ and the ratio P/P_{exc}; the resulting curves appear as solid lines in Fig. 4(a). Figure 4(b) shows $\gamma_{b\downarrow}(0)$ versus T. Between 5 and 50 K, $\gamma_{b\downarrow}(0)$ increases by more than two orders of magnitude.

At this stage, one may naturally wonder if local heating due to the optical excitation can explain the systematic increase in the spin-flip rate for large P_{exc}. To check this, we monitored possible spectral shifts of the X line during the measurements. At 5 K, on the whole power range (50 nW-30 μW), we observed a redshift of 35 pm from which we infer a maximum temperature increase of 0.5 K, far too small to explain the observed increase in the spin-flip rate. Possible mechanisms will be briefly discussed in the end of the article.

This section demonstrates that polarization measurements constitute a powerful probe of spin-flip processes. In particular, they give access to a global spin-flip rate over a broad range of excitation powers from the zero-power limit and up to the saturation of the excitonic emission. The latter regime cannot be easily accessed with time-resolved measurements, which are typically performed with low-excitation powers to avoid "reservoir effects" associated with the population of higher-energy levels. Nevertheless, time-resolved measurements enable to disentangle the contributions of γ_b and $\gamma_{\downarrow,\uparrow}$, at least, in the low-power regime. Therefore, they offer complementary insights on spin-flip processes as illustrated in the next section.

II. TIME-RESOLVED MEASUREMENTS

To perform time-resolved measurements, the Ti:sapphire laser is operated in a pulsed mode (pulse temporal full width at half maximum (FWHM), 200 fs; repetition rate, 76 MHz). On the detection side, temporal resolution is provided by a silicon APD. We determined the instrument response (IRF) of the setup using the pulsed laser tuned to 920 nm and properly attenuated. The measured IRF is shown as a dashed line in Fig. 5; it yields a time jitter (FWHM) of 450 ps. The IRF is systematically included in the analysis of experimental data.

A. Time decay of the biexciton emission

We first consider the decay of the XX emission line, a measurement that contributes to the determination of the photonic parameters. The excitation power is kept low enough to ensure an XX population that is roughly 10% of the saturation value. One can then neglect reservoir effects associated with the decay of higher-energy levels. After an instantaneous excitation, the XX population then decays with the radiative rate $\Gamma_{XX} = \Gamma_H + \Gamma_V = \Gamma_x + \Gamma_y$. A measurement performed at $T = 5$ K is shown in Fig. 5. The experimental data are fitted to a single-exponential decay function that is convoluted with the IRF: This yields $\Gamma_{XX} = 1.30 \pm 0.02$ ns^{-1}.

B. Time decay of the excitonic emission

1. Theoretical background

This theoretical section provides some background to illustrate the impact of spin flips on the time decay of excitonic populations. We consider an instantaneous and balanced excitation of the four excitonic states: at $t = 0$, $n_H(0) = n_V(0) = n_{D_h}(0) = n_{D_v}(0) = n_0$. The excitation power is kept sufficiently small to ensure that $n_0 \ll 1$, leading to a vanishingly small population of the biexiton state [$n_{XX}(0) = 0$]. The excitonic populations evolve according to

$$\frac{d}{dt}\begin{pmatrix} n_H \\ n_V \\ n_{\Sigma D} \\ n_{\Delta D} \end{pmatrix} = \begin{pmatrix} -\Gamma'_H & \gamma_b & \gamma_\uparrow & 0 \\ \gamma_b & -\Gamma'_V & \gamma_\uparrow & 0 \\ 2\gamma_\downarrow & 2\gamma_\downarrow & -2\gamma_\uparrow & 0 \\ 0 & 0 & 0 & -2\gamma_{d\uparrow} \end{pmatrix}\begin{pmatrix} n_H \\ n_V \\ n_{\Sigma D} \\ n_{\Delta D} \end{pmatrix}, \tag{14}$$

with $n_{\Sigma D} = n_{D_h} + n_{D_v}$, $n_{\Delta D} = n_{D_h} - n_{D_v}$ and $\Gamma'_{H,V} = \Gamma_{H,V} + 2\gamma_\downarrow + \gamma_b$. The equation governing the imbalance of the dark state populations is decoupled from the others and yields $n_{\Delta D}(t) = 0$ for equal initial populations. The remaining populations evolve according to

$$\begin{pmatrix} n_H \\ n_V \\ n_{\Sigma D} \end{pmatrix} = \alpha_1 \mathbf{V}_1 e^{-\Gamma_1 t} + \alpha_2 \mathbf{V}_2 e^{-\Gamma_2 t} + \alpha_3 \mathbf{V}_3 e^{-\Gamma_3 t}. \tag{15}$$

The decay rates Γ_i ($i = 1$–3) are the opposite of the eigenvalues of the 3×3 block matrix which appears in Eq. (14); $\mathbf{V}_i$ is the eigenvector associated with the eigenvalue $-\Gamma_i$; the coefficients α_i are fixed by initial conditions. In Appendix B, we employ first-order perturbation theory to provide analytical expressions in three limit cases: (i) slow spin flips ($\gamma_b,\ \gamma_{\downarrow,\uparrow} \ll \Gamma_{H,V}$), fast bright-bright and slow dark-bright spin-flips ($\gamma_b \gg \Gamma_{H,V} \gg \gamma_{\downarrow,\uparrow}$) and (iii) fast spin-flips ($\gamma_b,\ \gamma_{\downarrow,\uparrow} \gg \Gamma_{H,V}$). We will illustrate some of these cases directly on the experimental results. Our measurements are also resolved in polarization (along the x and y directions). The corresponding intensities $I_x(t)$ and $I_y(t)$ are given by Eqs. (4) and (5) by replacing steady-state populations by time-dependent ones.

2. Experimental results

Figure 6 shows the time-decay of the X line for the x and y polarization directions. The measurement has been repeated for sample holder temperatures ranging from $T = 5$ and up to 50 K. We first discuss the data corresponding to the lowest temperature. Both curves feature a multiexponential decay. In addition, the dominant initial decays for x and y channels are markedly different. From these observations we can conclude that such measurements are in or close to the slow spin-flip regime discussed in Appendix B ($\gamma_b,\ \gamma_{\downarrow,\uparrow} \ll \Gamma_{H,V}$). For moderate θ (which is the case here), the fast decay on channel x is dominated by Γ_H, whereas the fast decay on channel y is dominated by Γ_V. The long-time tail can be directly ascribed to the spin flips form dark to bright excitons with a rate dominated by $2\gamma_\uparrow$. In addition, there is no large difference between the time-integrated intensities of x and y channels. These observations are fully consistent with the measurements of a modest degree of linear polarization in the low-power regime.

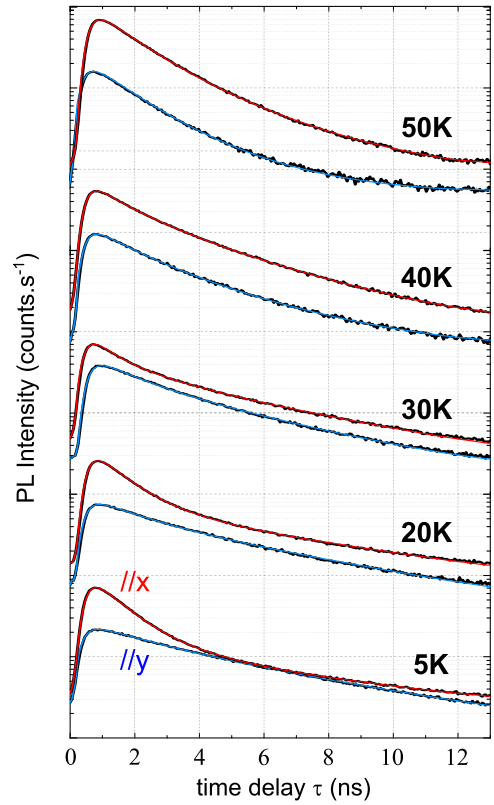

FIG. 6. Time-resolved decay of the excitonic emission line (log-lin plot). The measurements are performed for temperatures ranging between 5 and 50 K. For each temperature, we present data for the polarization directions x and y. The data are fitted to a triple exponential decay function that is convoluted with the measured IRF of the setup (see the text for details).

Increasing the temperature changes both the time dynamics and the relative intensities of the x and y decay curves. As the sample temperature increases, we make the following observations: (i) The decay curves remain multiexponential. (ii) The rates of the fast initial decays of x and y channels become identical. (iii) The long-time decay rate increases with the temperature. (iv) The time-integrated intensities associated with x and y channels become very different: Most of the light is emitted along the x photonic channel. These observations point towards increased spin-flip rates at higher temperatures. Of course, this global trend is no surprise and confirms the polarization analysis conducted in the first part of the article. Nevertheless, time-resolved measurements offer a key additional insight as they enable to separate the various spin-flip contributions. In particular, experimental results suggest that γ_b increases at a fast pace with T to exceed the radiative rates. $\gamma_\downarrow$ and $\gamma_\uparrow$ also increase, albeit slowly, and remain below the radiative recombination rates. This situation corresponds to the intermediate case discussed in Appendix B.

We now turn to a quantitative analysis. The time-dependent intensity is first fitted to $I_0 f(t) * \mathrm{IRF}(t) + d$. Here, $f(t) = \sum_i a_i e^{-i\Gamma_i t}$ is a triple-exponential decay function; the decay rates satisfy $\Gamma_1 > \Gamma_2 > \Gamma_3$, and the weights are linked by the normalization condition $a_1 + a_2 + a_3 = 1$. IRF(t) is the measured instrument response function, normalized so that

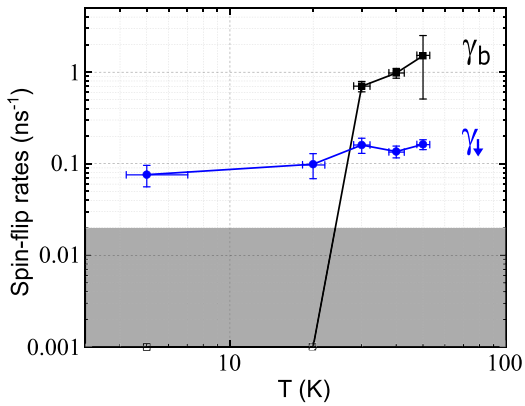

FIG. 7. Spin-flip rates γ_b and $\gamma_\downarrow$ as deduced from the time-resolved experiments shown in Fig. 6 (log-lin scale). The analysis detailed in the text yields $\gamma_\uparrow \approx \gamma_\downarrow$; for $T = 5$ and 20 K, one obtains γ_b below 0.02 ns^{-1}, the error bar in the slow bright-bright spin-flip regime (shaded area).

$\max[\mathrm{IRF}(t)] = 1$. I_0 is a global intensity scaling factor, and d is a constant dark count rate. The model presented in the previous paragraph is used to constrain the values of the exponential weights. The fit parameters $\{\Gamma_i\}$ and $\{a_i\}$ are listed in Appendix C. At 5 K, we obtain $\Gamma_1 - \Gamma_2 \approx \Gamma_H - \Gamma_V = 0.66 \pm 0.02$ ns^{-1}. Combined with the measured L_{XX}, this yields $\Gamma_H = 0.98 \pm 0.02$ and $\Gamma_V = 0.32 \pm 0.01$ ns^{-1}. By diagonalizing the 3×3 matrix which appears in Eq. (14) and using an optimization routine, we next determine the set of spin-flip rates $\{\gamma_b, \gamma_\downarrow, \gamma_\uparrow\}$ which better approaches the set of experimental decay rates $\{\Gamma_1, \Gamma_2, \Gamma_3\}$. Because of trace invariance, this inversion process hinges on two independent rates; we choose γ_b and $\gamma_\uparrow$. Furthermore, we impose the natural physical condition $\gamma_\downarrow \geqslant \gamma_\uparrow$. We repeat this procedure for x and y polarizations and discuss in the following the average rates deduced from these two measurements.

Figure 7 shows the spin-flip rates deduced from time-resolved measurements as a function of the temperature. Our analysis systematically yields $\gamma_\uparrow \approx \gamma_\downarrow$. At $T = 5$ K, spin flips are dominated by dark-bright spin flips: $\gamma_{\uparrow,\downarrow} = 0.08 \pm 0.02$ ns^{-1} and $\gamma_b < 0.02$ ns^{-1} (the optimization routine yields a vanishingly small γ_b, this upper limit corresponds to the error bar in the slow bright-bright spin-flip regime). In turn, these rates remain small as compared to the radiative decay rates. At $T = 50$ K, the rate hierarchy is completely reversed because of a dramatic increase in γ_b. In contrast $\gamma_\uparrow$ and $\gamma_\downarrow$ only show a relatively weak temperature dependence. Thus, the superlinear increase in $\gamma_{b\downarrow} = \gamma_b + \gamma_\downarrow$ with T observed with polarization measurements [see Fig. 4(b)] can be traced back to the fast increase in γ_b. Polarization and time-resolved measurements yield similar temperature dependencies for $\gamma_{b\downarrow}$. However, the values deduced from time-resolved measurements are systematically slightly larger than the one extracted from polarization data. This is consistent with the fact that in the latter case, we extrapolate a zero-power limit, whereas for time-resolved measurements, the excitation power is small but remains finite.

Our QD model captures the essential physics at play with a limited number of spin-flip rates. It could, nevertheless, be improved in the future. We suspect some approximations explain why our analysis yields $\gamma_\uparrow \approx \gamma_\downarrow$, despite a significant bright-dark energy separation (typically 200–300 μeV for the small InAs QDs investigated in this paper). In particular, at 5 K, the large-delay behavior of time-resolved data features distinct decay rates for x and y channels (Fig. 6). An obvious refinement would be to distinguish two sets of dark-to-bright spin-flip channels $|D_{h,v}\rangle \rightarrow |H\rangle$ and $|D_{h,v}\rangle \rightarrow |V\rangle$ with two distinct rates. Similar considerations hold for bright-to-dark spin-flip processes. For consistency, one should also introduce two rates for direct bright-bright spin flips. This finer description would, however, come at a price: To determine the six spin-flip rates, one should inject *a priori* relations between the spin-flip rates which, in turn, require a detailed understanding of the processes at play. As discussed in the next section, such a detailed understanding requires additional experimental investigations.

III. DISCUSSION AND CONCLUDING REMARKS

We summarize below the main experimental results:

(i) In the low-excitation limit and at low-temperature ($T = 5$ K), bright-bright spin flips are negligible: $\gamma_b < 0.02$ ns^{-1}. Dark-bright spin-flip rates are on the order of 0.1 ns^{-1} and remain much slower than the radiative decays ($\sim$1 ns^{-1}). As temperature increases, γ_b increases very strongly, at a much faster pace than $\gamma_{\downarrow,\uparrow}$. At 50 K, the rate hierarchy is already completely reversed: $\gamma_b > \Gamma_{H,V} > \gamma_{\downarrow,\uparrow}$.

(ii) The spin-flip rate (γ_b or $\gamma_{\uparrow,\downarrow}$) dramatically increases with the pumping power. Between the low-excitation regime ($P_{\mathrm{exc}} = 50$ nW) and the saturation of the excitonic emission ($P_{\mathrm{exc}} = 30$ μW), the spin-flip rate increases by two orders of magnitude. This effect is not due to an elevation of the temperature induced by the optical excitation.

We propose below a possible interpretation of our results. Acoustic phonons represent a natural candidate to accommodate for energy exchanges associated with excitonic spin flips. A single-phonon process can mediate dark-bright spin flips [12]. The fast increase in γ_b with T suggests that a higher-order process is at play for bright-bright spin flips, for example, the two-phonon process proposed in Ref. [11]. In our paper, the increase in the spin-flip rate with the excitation power is not due to an increase in the lattice temperature. However, it could be attributed to nonequilibrium phonons. These are created by the relaxation of hot carriers generated by the nonresonant optical excitation [32]. Their population is governed by a complex relaxation cascade, which involves phonon-phonon scattering processes. The associated scattering rate strongly decreases when the phonon energy decreases [33], enabling the buildup of a significant population of low-energy phonons which can affect the lifetime of spin states [34,35]. Alternatively, the power dependence of the spin-flip rate could be explained by Coulomb scattering involving carriers in the QD environment [36,37]. Further experiments—beyond the scope of this paper—are required to conclude this point.

Spin-flip processes represent a nuisance for quantum light emission. In particular, such processes have a negative impact on the spectral coherence of single-photon sources as

random jumps between the two bright excitons spoil the indistinguishability of the emitted photons. Of course, modern high-performance single-photon sources employ resonant excitation to reduce the time jitter in the emission of photons and to minimize the excitation of unwanted sources of noise in the QD environment [38–40]. Nevertheless, a faint nonresonant excitation is very often employed to stabilize the charge environment of the QD [41]. Our findings shows that care should be taken to optimize the photon indistinguishability.

Spin-flip processes also have a bright side and can sometimes be considered as a resource. As a first example, some of us recently introduced an all-optical method to map the position of single QDs embedded in a nanowire section [31]. In the case of a neutral QD, a fast spin flip was also required to enable the mapping. This can be achieved either by using a large nonresonant driving power or by increasing the temperature. A second, important situation is the efficient emission of photons in a well-controlled polarized mode. It can be achieved by embedding the QD in an anisotropic photonic structure as shown with waveguides [9,42,43] or microcavities [44,45]. When the eigenaxes of a neutral QD are approximately aligned with the photonic eigenaxes, spin-flip processes that are faster than radiative decays are mandatory to achieve polarized emission under nonresonant excitation [9]. We finally note that the optical anisotropy required to achieve polarization control can conversely be exploited to reveal spin-flip processes. In particular, the method demonstrated in this paper could be implemented with anisotropic optical cavities [44–47]. As an alternative to monolithic devices, semiopen microcavities offer an appealing spectral tunability [48], which can be combined with strain tuning of the mode splitting [49].

To conclude, we have proposed and demonstrated a method to probe spin flips between the excitonic states hosted by a neutral QD. By inserting the emitter in a photonic structure that features a pronounced optical anisotropy, we generate an imbalance between the radiative decay rates of the two bright excitons. Bright-bright and dark-bright spin flips can then be simply revealed by polarization measurements. Furthermore, time-resolved measurements allow to distinguish the contributions of these two processes in the low-excitation regime. We have presented and discussed the impact of the temperature and the one of the nonresonant excitation power. Our findings have implications for spontaneous emission control in anisotropic photonic environments as well as for the development of high-performance sources of quantum light.

ACKNOWLEDGMENTS

We warmly thank L. Besombes, H. Boukari, N. Chauvin, L. Lanco, J.-P. Poizat, and V. Voliotis for fruitful discussions. We also thank the two anonymous reviewers for their insightful and constructive comments. This work was supported by the French National Research Agency (Project No. IPOD ANR-19-CE47-0009-02). S.K. acknowledges funding from the European Union's Horizon 2020 Research and Innovation Programme under the Marie Sklodowska-Curie Grant Agreement No. 754303 and the Agence Nationale de la Recherche under the Programme "Investissements d'avenir" (Grant No. ANR-15-IDEX-02). Sample fabrication was carried out in the "Plateforme Technologique Amont" and in CEA/LETI/DOPT clean rooms.

APPENDIX A: STEADY-STATE POPULATIONS

The QD populations evolve according to the underdetermined rate equation system,

$$\begin{pmatrix} \dot{n}_{XX} \\ \dot{n}_H \\ \dot{n}_V \\ \dot{n}_{D_h} \\ \dot{n}_{D_v} \end{pmatrix} = \begin{pmatrix} -\Gamma_{XX} & P & P & P & P & 0 \\ \Gamma_H & -\Gamma_H - 2\gamma_\downarrow - \gamma_b - P & \gamma_b & \gamma_\uparrow & \gamma_\uparrow & \frac{1}{4}P \\ \Gamma_V & \gamma_b & -\Gamma_V - 2\gamma_\downarrow - \gamma_b - P & \gamma_\uparrow & \gamma_\uparrow & \frac{1}{4}P \\ 0 & \gamma_\downarrow & \gamma_\downarrow & -2\gamma_\uparrow - \gamma_d - P & \gamma_d & \frac{1}{4}P \\ 0 & \gamma_\downarrow & \gamma_\downarrow & \gamma_d & -2\gamma_\uparrow - \gamma_d - P & \frac{1}{4}P \end{pmatrix} \begin{pmatrix} n_{XX} \\ n_H \\ n_V \\ n_{D_h} \\ n_{D_v} \\ n_G \end{pmatrix}, \tag{A1}$$

which is completed by the conservation of the total QD population,

$$n_{XX} + n_H + n_V + n_{D_h} + n_{D_v} + n_G = 1. \tag{A2}$$

We introduce the new variables: $n_{\Sigma B} = n_H + n_V$, $n_{\Delta B} = n_H - n_V$, $n_{\Sigma D} = n_{D_h} + n_{D_v}$, and $n_{\Delta D} = n_{D_h} - n_{D_v}$. The steady-state populations are noted with a top bar and satisfy

$$\begin{pmatrix} 0 \\ 0 \\ 0 \\ 0 \\ 0 \\ 1 \end{pmatrix} = \begin{pmatrix} -1 & 0 & p & p & 0 & 0 \\ \Delta\widetilde{\Gamma} & -\frac{1}{2} - 2\widetilde{\gamma}_{b\downarrow} - p & -\frac{1}{2}\Delta\widetilde{\Gamma} & 0 & 0 & 0 \\ 1 & -\frac{1}{2}\Delta\widetilde{\Gamma} & -\frac{1}{2} - 2\widetilde{\gamma}_{\downarrow} - p & 2\widetilde{\gamma}_{\uparrow} & 0 & \frac{1}{2}p \\ 0 & 0 & 2\widetilde{\gamma}_{\downarrow} & -2\widetilde{\gamma}_{\uparrow} - p & 0 & \frac{1}{2}p \\ 0 & 0 & 0 & 0 & -2\widetilde{\gamma}_{d\uparrow} - p & 0 \\ 1 & 0 & 1 & 1 & 0 & 1 \end{pmatrix} \begin{pmatrix} \bar{n}_{XX} \\ \bar{n}_{\Delta B} \\ \bar{n}_{\Sigma B} \\ \bar{n}_{\Sigma D} \\ \bar{n}_{\Delta D} \\ \bar{n}_G \end{pmatrix}. \tag{A3}$$

Here, all rates have been normalized to $\Gamma_{XX} = \Gamma_H + \Gamma_V$. Except the normalized pumping rate $p = P/\Gamma_{XX}$, all normalized rates are noted with a tilde symbol (for example, $\widetilde{\gamma}_{\uparrow} = \gamma_{\uparrow}/\Gamma_{XX}$). We have also introduced $\Delta\widetilde{\Gamma} = \widetilde{\Gamma}_H - \widetilde{\Gamma}_V$, $\widetilde{\gamma}_{b\downarrow} = \widetilde{\gamma}_b + \widetilde{\gamma}_{\downarrow}$, and $\widetilde{\gamma}_{d\uparrow} = \widetilde{\gamma}_d + \widetilde{\gamma}_{\uparrow}$. The equation governing $\bar{n}_{\Delta D}$ is decoupled from the other ones and yields $\bar{n}_{\Delta D} = 0$. The remaining system does not depend on γ_d.

To determine L_X, it is sufficient to calculate the population ratio,

$$\frac{\bar{n}_H}{\bar{n}_V} = \frac{\bar{n}_{\Sigma B} + \bar{n}_{\Delta B}}{\bar{n}_{\Sigma B} - \bar{n}_{\Delta B}}. \tag{A4}$$

In turn, this ratio only depends on $\bar{n}_{\Delta B}/\bar{n}_{\Sigma B}$, which is determined from Eq. (A3) and reads

$$\frac{\bar{n}_{\Delta B}}{\bar{n}_{\Sigma B}} = \Delta\widetilde{\Gamma}\frac{-(2\widetilde{\gamma}_{\uparrow} + p) + 2p\left(\frac{1}{4} + 2\widetilde{\gamma}_{\updownarrow} + p\right)}{(2\widetilde{\gamma}_{\uparrow} + p)(1 + 4\widetilde{\gamma}_{b\downarrow} + 2p) - \frac{1}{2}\Delta\widetilde{\Gamma}^2 p}. \tag{A5}$$

Simpler expressions can be obtained in the low and large pumping regimes. In the low-power regime ($P \ll \Gamma_{H,V}, \gamma_b, \gamma_{\uparrow,\downarrow}$),

$$\frac{\bar{n}_H}{\bar{n}_V} = \frac{\Gamma_V + 2\gamma_{b\downarrow}}{\Gamma_H + 2\gamma_{b\downarrow}} \tag{A6}$$

$$= \frac{\sin^2(\theta)\Gamma_x + \cos^2(\theta)\Gamma_y + 2\gamma_{b\downarrow}}{\cos^2(\theta)\Gamma_x + \sin^2(\theta)\Gamma_y + 2\gamma_{b\downarrow}}. \tag{A7}$$

Note we came back to unormalized rates. In the large pumping regime ($P \gg \Gamma_{H,V}$),

$$\frac{\bar{n}_H}{\bar{n}_V} = \frac{(\Gamma_x + \Gamma_y) + \cos(2\theta) f(P)(\Gamma_x - \Gamma_y)}{(\Gamma_x + \Gamma_y) - \cos(2\theta) f(P)(\Gamma_x - \Gamma_y)}, \tag{A8}$$

where $f(P)$ is given by Eq. (12) in the main text.

APPENDIX B: TIME-RESOLVED DYNAMICS

In this Appendix, we employ first-order perturbation theory to derive approximate expressions for the decay rates Γ_1, Γ_2, and Γ_3 and for the excitonic populations $n_H(t)$, $n_V(t)$, and $\Sigma n_D(t)$. For simplicity the common multiplying factor n_0 is omitted. We also briefly discuss the various contributions to $n_H(t)$ and $n_V(t)$.

1. Slow spin flips

We first consider the case where spin-flip processes are much slower than the radiative decays ($\gamma_b, \gamma_{\uparrow,\downarrow} \ll \Gamma_{H,V}$). In these conditions,

$$\Gamma_1 = \Gamma_H + \gamma_b + 2\gamma_{\downarrow}, \tag{B1}$$

$$\Gamma_2 = \Gamma_V + \gamma_b + 2\gamma_{\downarrow}, \tag{B2}$$

$$\Gamma_3 = 2\gamma_{\uparrow}. \tag{B3}$$

Following our hypotheses, we have the hierarchy $\Gamma_1 > \Gamma_2 \gg \Gamma_3$. To first order, $\Gamma_1 - \Gamma_2 = \Gamma_H - \Gamma_V$, a result used in the main text to determine θ. Within a common constant factor, the populations decay as

$$n_H(t) = +\left(1 - \frac{\gamma_b}{\Delta\Gamma} - \frac{2\gamma_{\uparrow}}{\Gamma_H}\right)e^{-\Gamma_1 t} + \left(\frac{\gamma_b}{\Delta\Gamma}\right)e^{-\Gamma_2 t} + \left(\frac{2\gamma_{\uparrow}}{\Gamma_H}\right)e^{-\Gamma_3 t}, \tag{B4}$$

$$n_V(t) = -\left(\frac{\gamma_b}{\Delta\Gamma}\right)e^{-\Gamma_1 t} + \left(1 + \frac{\gamma_b}{\Delta\Gamma} - \frac{2\gamma_{\uparrow}}{\Gamma_V}\right)e^{-\Gamma_2 t} + \left(\frac{2\gamma_{\uparrow}}{\Gamma_V}\right)e^{-\Gamma_3 t}, \tag{B5}$$

$$n_{\Sigma D}(t) = -\left(\frac{2\gamma_{\downarrow}}{\Gamma_H}\right)e^{-\Gamma_1 t} - \left(\frac{2\gamma_{\downarrow}}{\Gamma_V}\right)e^{-\Gamma_2 t} + \left(2 + \frac{2\gamma_{\downarrow}}{\Gamma_H} + \frac{2\gamma_{\downarrow}}{\Gamma_V}\right)e^{-\Gamma_3 t}, \tag{B6}$$

with $\Delta\Gamma = \Gamma_H - \Gamma_V$. At leading order, $n_H(t)$ is dominated by the term associated with $\Gamma_1 \approx \Gamma_H$. Bright-bright spin flips result in a small mixing of the populations of levels $|H\rangle$ and $|V\rangle$. This leads to a first-order correction associated with $\Gamma_2 \approx \Gamma_V$. The slow dark-to-bright spin flips also induce a small population mixing between $|H\rangle$ and the dark states. This results in a perturbative term associated with the slow decay rate $\Gamma_3 \approx 2\gamma_{\uparrow}$. Similar considerations hold for $n_V(t)$ (one then has to exchange the roles of Γ_1 and Γ_2 terms).

2. Fast bright-bright spin flips and slow bright-dark spin flips

We next consider an intermediate situation: $\gamma_b \gg \Gamma_{H,V} \gg \gamma_{\uparrow,\downarrow}$. The three decay rates read

$$\Gamma_1 = 2\gamma_b + \frac{\Gamma_H + \Gamma_V}{2} + 2\gamma_{\downarrow}, \tag{B7}$$

$$\Gamma_2 = \frac{\Gamma_H + \Gamma_V}{2} + 2\gamma_{\downarrow}, \tag{B8}$$

$$\Gamma_3 = 2\gamma_{\uparrow}. \tag{B9}$$

Following our hypotheses, we have the hierarchy $\Gamma_1 \gg \Gamma_2 \gg \Gamma_3$. The populations decay as

$$n_H(t) = +\left(\frac{\Delta\Gamma}{4\gamma_b}\right)e^{-\Gamma_1 t} + \left(1 - \frac{4\gamma_\uparrow}{\Sigma\Gamma} - \frac{\Delta\Gamma}{4\gamma_b}\right)e^{-\Gamma_2 t} + \left(\frac{4\gamma_\uparrow}{\Sigma\Gamma}\right)e^{-\Gamma_3 t}, \tag{B10}$$

$$n_V(t) = -\left(\frac{\Delta\Gamma}{4\gamma_b}\right)e^{-\Gamma_1 t} + \left(1 - \frac{4\gamma_\uparrow}{\Sigma\Gamma} + \frac{\Delta\Gamma}{4\gamma_b}\right)e^{-\Gamma_2 t} + \left(\frac{4\gamma_\uparrow}{\Sigma\Gamma}\right)e^{-\Gamma_3 t}, \tag{B11}$$

$$n_{\Sigma D}(t) = -2\left(\frac{4\gamma_\downarrow}{\Sigma\Gamma}\right)e^{-\Gamma_2 t} + 2\left(1 + \frac{4\gamma_\downarrow}{\Sigma\Gamma}\right)e^{-\Gamma_3 t}, \tag{B12}$$

with $\Sigma\Gamma = \Gamma_H + \Gamma_V$. At leading (i.e., zero) order, the time evolution of $n_H(t)$ and $n_V(t)$ are identical and dominated by the term associated with $\Gamma_2 \approx (\Gamma_H + \Gamma_V)/2$. The fast bright-bright spin flips lead to an averaging over the two radiative decay channels. The terms associated with the fast equilibration of the populations of $|H\rangle$ and $|V\rangle$ with a rate $\Gamma_1 \approx 2\gamma_b$ are only present as a perturbation because the two initial populations are identical. Finally, the term associated with $\Gamma_3 \approx 2\gamma_\uparrow$ is a first-order perturbation. It results in a slow decay tail associated with the spin-flips from dark to bright excitons.

3. Fast spin flips

We finally consider the case where all spin-flip processes are much faster than radiative decays: $\gamma_b,\ \gamma_{\uparrow,\downarrow} \gg \Gamma_{H,V}$. The decay rates read

$$\Gamma_1 = 2(\gamma_b + \gamma_\downarrow) + \frac{\Gamma_H + \Gamma_V}{2}, \tag{B13}$$

$$\Gamma_2 = 2(\gamma_\uparrow + \gamma_\downarrow) + \frac{\gamma_\downarrow}{\gamma_\uparrow + \gamma_\downarrow}\frac{\Gamma_H + \Gamma_V}{2}, \tag{B14}$$

$$\Gamma_3 = \frac{\gamma_\uparrow}{\gamma_\uparrow + \gamma_\downarrow}\frac{\Gamma_H + \Gamma_V}{2}, \tag{B15}$$

with the rate hierarchy $\Gamma_1, \Gamma_2 \gg \Gamma_3$. Because complete expressions of populations are quite bulky, we only give the leading zero-order terms. In the following, the notation $O_{i,j}(\Gamma/\gamma)$ designates first-order corrections (Γ is a radiative rate, and γ is a spin-flip rate, $\Gamma/\gamma \ll 1$),

$$n_H(t) = O_{H,1}(\Gamma/\gamma)e^{-\Gamma_1 t} + \left(\frac{\gamma_\downarrow - \gamma_\uparrow}{\gamma_\updownarrow} + O_{H,2}(\Gamma/\gamma)\right)e^{-\Gamma_2 t} + \left(\frac{2\gamma_\uparrow}{\gamma_\updownarrow} + O_{H,3}(\Gamma/\gamma)\right)e^{-\Gamma_3 t}, \tag{B16}$$

$$n_V(t) = O_{V,1}(\Gamma/\gamma)e^{-\Gamma_1 t} + \left(\frac{\gamma_\downarrow - \gamma_\uparrow}{\gamma_\updownarrow} + O_{V,2}(\Gamma/\gamma)\right)e^{-\Gamma_2 t} + \left(\frac{2\gamma_\uparrow}{\gamma_\updownarrow} + O_{V,3}(\Gamma/\gamma)\right)e^{-\Gamma_3 t}, \tag{B17}$$

$$n_{\Sigma D}(t) = 2\left(\frac{\gamma_\uparrow - \gamma_\downarrow}{\gamma_\updownarrow} + O_{\Sigma D,2}(\Gamma/\gamma)\right)e^{-\Gamma_2 t} + 2\left(\frac{2\gamma_\downarrow}{\gamma_\updownarrow} + O_{\Sigma D,3}(\Gamma/\gamma)\right)e^{-\Gamma_3 t}, \tag{B18}$$

with $\gamma_\updownarrow = \gamma_\downarrow + \gamma_\uparrow$. At leading order, $n_H(t)$ and $n_V(t)$ feature identical time dependence. The term associated with the fast decay $\Gamma_2 \approx 2(\gamma_\uparrow + \gamma_\downarrow)$ corresponds to the equilibration of the bright and dark exciton populations. It is present at leading order because, in general, the initial conditions do not correspond to the equilibrium values set by the rates $\gamma_\uparrow$ and $\gamma_\downarrow$. The last term, associated with $\Gamma_3 = \frac{1}{2}(\gamma_\uparrow/\gamma_\updownarrow)(\Gamma_H + \Gamma_V)$, is dominated by the slow radiative decay. The fast spin flips between bright excitons lead to an averaging over the two radiative decay channels. The dark-to-bright spin flips lead to an additional reduction by a factor $\gamma_\uparrow/(\gamma_\downarrow + \gamma_\uparrow)$, the fraction of time spent in a bright state. In the high-temperature limit, $\gamma_\uparrow \approx \gamma_\downarrow$ and $\Gamma_3 \approx (\Gamma_H + \Gamma_V)/4$.

APPENDIX C: FIT PARAMETERS OF TIME-RESOLVED DATA

See Table I.

TABLE I. Decay rates $\{\Gamma_i\}$ and weights $\{a_i\}$ obtained from the fit of polarization- and time-resolved measurements of the excitonic emission (tag "Fit"). As described in the main text, we determine the set of spin-flip rates $\{\gamma_b, \gamma_\downarrow, \gamma_\uparrow\}$ that better approach the set of fitted decay rates within the model developed in Sec. II B 1. The associated decay rates and weights appear under the tag "Inv".

		p		x			y	
		i	1	2	3	1	2	3
5 K	Fit	Γ_i (ns^{-1})	1.15	0.48	0.11	1.15	0.48	0.14
		a_i	0.76	0.14	0.10	−0.04	0.55	0.49
	Inv	Γ_i (ns^{-1})	1.14	0.50	0.11	1.15	0.51	0.11
		a_i	0.81	0.00	0.18	0.06	0.46	0.49
20 K	Fit	Γ_i (ns^{-1})	1.16	0.55	0.15	1.16	0.55	0.20
		a_i	0.71	0.13	0.16	0.12	0.31	0.57
	Inv	Γ_i (ns^{-1})	1.19	0.55	0.12	1.21	0.58	0.13
		a_i	0.78	−0.01	0.23	0.06	0.39	0.55
30 K	Fit	Γ_i (ns^{-1})	2.51	0.92	0.21	2.51	0.92	0.25
		a_i	0.35	0.32	0.33	−0.04	0.44	0.60
	Inv	Γ_i (ns^{-1})	2.45	1.01	0.18	2.45	1.05	0.18
		a_i	0.21	0.35	0.44	−0.12	0.52	0.60
40 K	Fit	Γ_i (ns^{-1})	2.99	0.78	0.30	2.99	0.78	0.30
		a_i	0.24	0.39	0.37	−0.10	0.56	0.54
	Inv	Γ_i (ns^{-1})	2.93	0.97	0.17	2.94	0.97	0.17
		a_i	0.16	0.44	0.41	−0.11	0.60	0.51
50 K	Fit	Γ_i (ns^{-1})	4.00	0.89	0.38	4.00	0.89	0.40
		a_i	0.07	0.62	0.31	−0.07	0.74	0.33
	Inv	Γ_i (ns^{-1})	4.02	1.07	0.18	4.04	1.09	0.19
		a_i	0.10	0.43	0.47	−0.08	0.51	0.56

[1] P. Lodahl, S. Mahmoodian, and S. Stobbe, Interfacing single photons and single quantum dots with photonic nanostructures, Rev. Mod. Phys. **87**, 347 (2015).

[2] M. Bayer, G. Ortner, O. Stern, A. Kuther, A. A. Gorbunov, A. Forchel, P. Hawrylak, S. Fafard, K. Hinzer, T. L. Reinecke, S. N. Walck, J. P. Reithmaier, F. Klopf, and F. Schäfer, Fine structure of neutral and charged excitons in self-assembled In(Ga)As/(Al)GaAs quantum dots, Phys. Rev. B **65**, 195315 (2002).

[3] P. Senellart, G. Solomon, and A. White, High-performance semiconductor quantum-dot single-photon sources, Nat. Nanotechnol. **12**, 1026 (2017).

[4] D. Huber, M. Reindl, J. Aberl, A. Rastelli, and R. Trotta, Semiconductor quantum dots as an ideal source of polarization-entangled photon pairs on-demand: A review, J. Opt. **20**, 073002 (2018).

[5] I. Schwartz, D. Cogan, E. R. Schmidgall, Y. Don, L. Gantz, O. Kenneth, N. H. Lindner, and D. Gershoni, Deterministic generation of a cluster state of entangled photons, Science **354**, 434 (2016).

[6] M. Paillard, X. Marie, P. Renucci, T. Amand, A. Jbeli, and J. M. Gérard, Spin Relaxation Quenching in Semiconductor Quantum Dots, Phys. Rev. Lett. **86**, 1634 (2001).

[7] W. Langbein, P. Borri, U. Woggon, V. Stavarache, D. Reuter, and A. D. Wieck, Radiatively limited dephasing in InAs quantum dots, Phys. Rev. B **70**, 033301 (2004).

[8] I. Favero, G. Cassabois, C. Voisin, C. Delalande, P. Roussignol, R. Ferreira, C. Couteau, J. P. Poizat, and J. M. Gérard, Fast exciton spin relaxation in single quantum dots, Phys. Rev. B **71**, 233304 (2005).

[9] M. Munsch, J. Claudon, J. Bleuse, N. S. Malik, E. Dupuy, J.-M. Gérard, Y. Chen, N. Gregersen, and J. Mørk, Linearly Polarized, Single-Mode Spontaneous Emission in a Photonic Nanowire, Phys. Rev. Lett. **108**, 077405 (2012).

[10] Q. Wang, S. Stobbe, H. Thyrrestrup, H. Hofmann, M. Kamp, T. W. Schlereth, S. Höfling, and P. Lodahl, Highly anisotropic decay rates of single quantum dots in photonic crystal membranes, Opt. Lett. **35**, 2768 (2010).

[11] E. Tsitsishvili and H. Kalt, Exciton spin relaxation in strongly confining semiconductor quantum dots, Phys. Rev. B **82**, 195315 (2010).

[12] J. Johansen, B. Julsgaard, S. Stobbe, J. M. Hvam, and P. Lodahl, Probing long-lived dark excitons in self-assembled quantum dots, Phys. Rev. B **81**, 081304(R) (2010).

[13] J. M. Smith, P. A. Dalgarno, R. J. Warburton, A. O. Govorov, K. Karrai, B. D. Gerardot, and P. M. Petroff, Voltage Control of the Spin Dynamics of an Exciton in a Semiconductor Quantum Dot, Phys. Rev. Lett. **94**, 197402 (2005).

[14] H. Kurtze, D. R. Yakovlev, D. Reuter, A. D. Wieck, and M. Bayer, Hyperfine interaction mediated exciton spin relaxation in (In,Ga)As quantum dots, Phys. Rev. B **85**, 195303 (2012).

[15] Z. L. Yuan, B. E. Kardynal, R. M. Stevenson, A. J. Shields, C. J. Lobo, K. Cooper, N. S. Beattie, D. A. Ritchie, and M. Pepper, Electrically driven single-photon source, Science **295**, 102 (2002).

[16] C. L. Salter, R. M. Stevenson, I. Farrer, C. A. Nicoll, D. A. Ritchie, and A. J. Shields, An entangled-light-emitting diode, Nature (London) **465**, 594 (2010).

[17] A. Schlehahn, A. Thoma, P. Munnelly, M. Kamp, S. Höfling, T. Heindel, C. Schneider, and S. Reitzenstein, An electrically driven cavity-enhanced source of indistinguishable photons with 61% overall efficiency, APL Photonics **1**, 011301 (2016).

[18] O. Labeau, P. Tamarat, and B. Lounis, Temperature Dependence of the Luminescence Lifetime of Single CdSe/ZnS Quantum Dots, Phys. Rev. Lett. **90**, 257404 (2003).

[19] J. Kasprzak, S. Portolan, A. Rastelli, L. Wang, J. D. Plumhof, O. G. Schmidt, and W. Langbein, Vectorial nonlinear coherent response of a strongly confined exciton-biexciton system, New J. Phys. **15**, 055006 (2013).

[20] J. Claudon, N. Gregersen, P. Lalanne, and J.-M. Gérard, Harnessing light with photonic nanowires: Fundamentals and applications to quantum optics, ChemPhysChem **14**, 2393 (2013).

[21] N. Gregersen, T. R. Nielsen, J. Claudon, J. M. Gérard, and J. Mørk, Controlling the emission profile of a nanowire with a conical taper, Opt. Lett. **33**, 1693 (2008).

[22] I. Friedler, P. Lalanne, J. P. Hugonin, J. Claudon, J. M. Gérard, A. Beveratos, and I. Robert-Philip, Efficient photonic mirrors for semiconductor nanowires, Opt. Lett. **33**, 2635 (2008).

[23] I. Friedler, C. Sauvan, J. P. Hugonin, P. Lalanne, J. Claudon, and J. M. Gérard, Solid-state single photon sources: The nanowire antenna, Opt. Express **17**, 2095 (2009).

[24] C. Böckler, S. Reitzenstein, C. Kistner, R. Debusmann, A. Löffler, T. Kida, S. Höfling, A. Forchel, L. Grenouillet, J. Claudon, and J. M. Gérard, Electrically driven high-Q quantum dot-micropillar cavities, Appl. Phys. Lett. **92**, 091107 (2008).

[25] Q. Ren, J. Lu, H. H. Tan, S. Wu, L. Sun, W. Zhou, W. Xie, Z. Sun, Y. Zhu, C. Jagadish, S. C. Shen, and Z. Chen, Spin-resolved purcell effect in a quantum dot microcavity system, Nano Lett. **12**, 3455 (2012).

[26] I. Favero, G. Cassabois, A. Jankovic, R. Ferreira, D. Darson, C. Voisin, C. Delalande, P. Roussignol, A. Badolato, P. M. Petroff, and J. M. Gérard, Giant optical anisotropy in a single InAs quantum dot in a very dilute quantum-dot ensemble, Appl. Phys. Lett. **86**, 041904 (2005).

[27] J. Bleuse, J. Claudon, M. Creasey, N. S. Malik, J.-M. Gérard, I. Maksymov, J.-P. Hugonin, and P. Lalanne, Inhibition, Enhancement, and Control of Spontaneous Emission in Photonic Nanowires, Phys. Rev. Lett. **106**, 103601 (2011).

[28] S. Cortez, O. Krebs, P. Voisin, and J. M. Gérard, Polarization of the interband optical dipole in inas gaas self-organized quantum dots, Phys. Rev. B **63**, 233306 (2001).

[29] C. Tonin, R. Hostein, V. Voliotis, R. Grousson, A. Lemaitre, and A. Martinez, Polarization properties of excitonic qubits in single self-assembled quantum dots, Phys. Rev. B **85**, 155303 (2012).

[30] J. Claudon, J. Bleuse, N. S. Malik, M. Bazin, P. Jaffrennou, N. Gregersen, C. Sauvan, P. Lalanne, and J.-M. Gérard, A highly efficient single-photon source based on a quantum dot in a photonic nanowire, Nat. Photonics **4**, 174 (2010).

[31] R. Fons, A. D. Osterkryger, P. Stepanov, E. Gautier, J. Bleuse, J.-M. Gérard, N. Gregersen, and J. Claudon, All-optical mapping of the position of quantum dots embedded in a nanowire antenna, Nano Lett. **18**, 6434 (2018).

[32] M. E. Msall and J. P. Wolfe, Phonon production in weakly photoexcited semiconductors: Quasidiffusion in Ge, GaAs, and Si, Phys. Rev. B **56**, 9557 (1997).

[33] A. A. Maznev, F. Hofmann, A. Jandl, K. Esfarjani, M. T. Bulsara, E. A. Fitzgerald, G. Chen, and K. A. Nelson, Lifetime

of sub-Thz coherent acoustic phonons in a GaAs-AlAs superlattice, Appl. Phys. Lett. **102**, 041901 (2013).

[34] A. Lafuente-Sampietro, H. Utsumi, M. Sunaga, K. Makita, H. Boukari, S. Kuroda, and L. Besombes, Dynamics of a Cr spin in a semiconductor quantum dot: Hole-Cr flip-flops and spin-phonon coupling, Phys. Rev. B **97**, 155301 (2018).

[35] V. Tiwari, K. Makita, M. Arino, M. Morita, S. Kuroda, H. Boukari, and L. Besombes, Influence of nonequilibrium phonons on the spin dynamics of a single Cr atom, Phys. Rev. B **101**, 035305 (2020).

[36] L. Besombes, Y. Léger, J. Bernos, H. Boukari, H. Mariette, J. P. Poizat, T. Clement, J. Fernández-Rossier, and R. Aguado, Optical probing of spin fluctuations of a single paramagnetic Mn atom in a semiconductor quantum dot, Phys. Rev. B **78**, 125324 (2008).

[37] D. Huber, M. Reindl, S. Filipe Covre da Silva, C. Schimpf, J. Martín-Sánchez, H. Huang, G. Piredda, J. Edlinger, A. Rastelli, and R. Trotta, Strain-Tunable GaAs Quantum Dot: A Nearly Dephasing-Free Source of Entangled Photon Pairs on Demand, Phys. Rev. Lett. **121**, 033902 (2018).

[38] Y.-M. He, Y. He, Y.-J. Wei, D. Wu, M. Atatüre, C. Schneider, S. Höfling, M. Kamp, C.-Y. Lu, and J.-W. Pan, On-demand semiconductor single-photon source with near-unity indistinguishability, Nat. Nanotechnol. **8**, 213 (2013).

[39] X. Ding, Y. He, Z.-C. Duan, N. Gregersen, M.-C. Chen, S. Unsleber, S. Maier, C. Schneider, M. Kamp, S. Höfling, C.-Y. Lu, and J.-W. Pan, On-Demand Single Photons with High Extraction Efficiency and Near-Unity Indistinguishability from a Resonantly Driven Quantum Dot in a Micropillar, Phys. Rev. Lett. **116**, 020401 (2016).

[40] N. Somaschi, V. Giesz, L. De Santis, J. C. Loredo, M. P. Almeida, G. Hornecker, S. L. Portalupi, T. Grange, C. Antón, J. Demory, C. Gómez, I. Sagnes, N. D. Lanzillotti-Kimura, A. Lemaître, A. Auffèves, A. G. White, L. Lanco, and P. Senellart, Near-optimal single-photon sources in the solid state, Nat. Photonics **10**, 340 (2016).

[41] H. S. Nguyen, G. Sallen, C. Voisin, P. Roussignol, C. Diederichs, and G. Cassabois, Optically Gated Resonant Emission of Single Quantum Dots, Phys. Rev. Lett. **108**, 057401 (2012).

[42] T. Ba Hoang, J. Beetz, L. Midolo, M. Skacel, M. Lermer, M. Kamp, S. Höfling, L. Balet, N. Chauvin, and A. Fiore, Enhanced spontaneous emission from quantum dots in short photonic crystal waveguides, Appl. Phys. Lett. **100**, 061122 (2012).

[43] P. Stepanov, A. Delga, X. Zang, J. Bleuse, E. Dupuy, E. Peinke, P. Lalanne, J.-M. Gérard, and J. Claudon, Quantum dot spontaneous emission control in a ridge waveguide, Appl. Phys. Lett. **106**, 041112 (2015).

[44] E. Moreau, I. Robert, J. M. Gérard, I. Abram, L. Manin, and V. Thierry-Mieg, Single-mode solid-state single photon source based on isolated quantum dots in pillar microcavities, Appl. Phys. Lett. **79**, 2865 (2001).

[45] S. Strauf, N. G. Stoltz, M. T. Rakher, L. A. Coldren, P. M. Petroff, and D. Bouwmeester, High-frequency single–photon source with polarization control, Nat. Photonics **1**, 704 (2007).

[46] H. Wang, Y.-M. He, T.-H. Chung, H. Hu, Y. Yu, S. Chen, X. Ding, M.-C. Chen, J. Qin, X. Yang, R.-Z. Liu, Z.-C. Duan, J.-P. Li, S. Gerhardt, K. Winkler, J. Jurkat, L.-J. Wang, N. Gregersen, Y.-H. Huo, Q. Dai *et al.*, Towards optimal single-photon sources from polarized microcavities, Nat. Photonics **13**, 770 (2019).

[47] F. Liu, A. J. Brash, J. O'Hara, L. M. P. P. Martins, C. L. Phillips, R. J. Coles, B. Royall, E. Clarke, C. Bentham, N. Prtljaga, I. E. Itskevich, L. R. Wilson, M. S. Skolnick, and A. M. Fox, High Purcell factor generation of indistinguishable on-chip single photons, Nat. Nanotechnol. **13**, 835 (2018).

[48] N. Tomm, A. Javadi, N. O. Antoniadis, D. Najer, M. C. Löobl, A. R. Korsch, R. Schott, S. R. Valentin, A. D. Wieck, A. Ludwig, and R. J. Warburton, A bright and fast source of coherent single photons, Nat. Nanotechnol. **16**, 399 (2021).

[49] N. Tomm, A. R. Korsch, A. Javadi, D. Najer, R. Schott, S. R. Valentin, A. D. Wieck, A. Ludwig, and R. J. Warburton, Tuning the Mode Splitting of a Semiconductor Microcavity with Uniaxial Stress, Phys. Rev. Appl. **15**, 054061 (2021).